Check for updates

Size-dependent formation of membrane nanotubes: continuum modeling and molecular dynamics simulations†

Falin Tian,[ab] Tongtao Yue, [ID][c] Wei Dong,[b] Xin Yi [ID] *[de] and Xianren Zhang [ID] *[a]

Membrane nanotubes play important functional roles in numerous cell activities such as cellular transport and communication. By exerting an external pulling force over a finite region in a membrane patch, here we investigate the size dependence of the membrane nanotube formation under the continuum and atomistic modeling frameworks. It is shown that the membrane undergoes a discontinuous shape transition as the size of the pulling region and the membrane tension increase. A formula characterizing the nonlinear relationship between the maximum static pulling force and pulling size is identified. During the membrane extraction, lipids in the upper and lower leaflets exhibit different behaviors of structural rearrangements. Moreover, our computational simulations indicate that the steady state pulling force increases linearly with the pulling velocity as well as the size of the pulling region.

1 Introduction

Membrane nanotubes, also known as membrane tethers, are ubiquitous in living cells and their organelles such as the endoplasmic reticulum,[1] mitochondria,[2] and Golgi apparatus,[3] and play important functional roles in numerous cell activities including intracellular trafficking, intercellular transport and communication,[4–6] and cell migration.[7,8] For example, the HIV-1 virus can spread through tubule interconnections between T cells.[6] Neutrophil rolling at high shear stress induces membrane tethers and slings which together contribute to forces balancing the hydrodynamic drag and stabilize the rolling cell.[8] Membrane nanotubes can be formed by exerting a localized pulling force upon the lipid membrane. The required force can be generated by the cooperative movement of motor proteins,[9] actin polymerization[10] or using hydrodynamical flows,[11,12] mechanical micropipettes,[13] optical or magnetic tweezers,[14–17] or the electrical microelectrode system.[18] Besides the application of an external force, the aggregation of BAR domain proteins[19] and nanoparticles[20–22] and the anchoring of polymers[23] on the lipid membrane, vesicle deflation[24] or even the compression of confined membranes[25] can induce tubular membrane protrusions of a similar highly curved structure to that of membrane tethers.

Both theoretical and experimental studies have been carried out to explore the mechanical behavior of tether formation and characterize the mechanical properties of membrane nanotubes such as the membrane tension, membrane viscosity, and inter-layer friction.[12,13,26–29] In the case of the membrane extraction at a constant membrane tension and low pulling velocity, the pulling force increases almost linearly with the pulling displacement in the early extraction stage, and then gradually rises to a peak which is followed by a drop to an equilibrium value upon the formation of a membrane nanotube of uniform radius.[15,16,27,28,30] Theoretical analysis on the equilibrium configuration of a cylindrical membrane nanotube leads to a simple relation connecting the equilibrium pulling force, nanotube radius, membrane tension and bending rigidity,[12,13,26–28] which has been widely employed to determine the membrane properties from the measured forces and tube radii.[9,26,30] As the pulling velocity increases, the effects of the membrane viscosity, inter-monolayer slip, and the possible membrane slip over the cytoskeleton on the membrane extraction become significant,[13,26,31] which enables the quantification of the effective membrane viscosity by manipulating tethers over a physiological range of tether extraction rates.[13–17,26] Recently, it has been demonstrated that molecular dynamics simulations can be employed to investigate the molecular structure and formation process of tethers and determine the

[a] *State Key Laboratory of Organic-Inorganic Composites, Beijing University of Chemical Technology, Beijing 100029, China. E-mail: zhangxr@mail.buct.edu.cn*

[b] *Laboratoire de Chimie, Ecole Normale Superieure de Lyon, 46 Allee d'Italie, 69364 Lyon Cedex 07, France*

[c] *State Key Laboratory of Heavy Oil Processing, Center for Bioengineering and Biotechnology, China University of Petroleum (East China), Qingdao 266580, China*

[d] *Department of Mechanics and Engineering Science, College of Engineering, Peking University, Beijing 100871, China*

[e] *Beijing Innovation Center for Engineering Science and Advanced Technology, Peking University, Beijing 100871, China. E-mail: xyi@pku.edu.cn*

† Electronic supplementary information (ESI) available: Supplemental figures about the force–extraction curve, membrane configurations, and energy variations are presented. See DOI: 10.1039/c7cp06212e

membrane viscosity, though the relationship between the pulling force and the membrane extraction has not yet been identified.[32] Besides studies on the extraction of purified lipid membranes, experiments on the tether formation from cells reveal insights into the mechanical behavior of cell membranes in the presence of the protein network underneath the membrane[29,33] or actin filaments within the extracted membrane nanotubes.[10,30]

Compared to the extensive experimental and theoretical investigations focusing on the tether formation and pulling behaviors of the membrane in the scenario of the point pulling force,[13,15–17,26–28,34] there have been no systematic studies on the size effect of the pulling region on membrane extraction under the continuum and atomistic modeling frameworks, except a few studies with a combination of experiments and Monte Carlo simulations in quasi-static pulling circumstances.[30,35] Additionally, detailed configurational and structural information about lipids in the deformed membrane and their relationship with the force–extraction curve have not been elucidated. In this work, we perform theoretical analysis and dissipative particle dynamics (DPD) simulations to investigate the physical mechanisms underlying the membrane nanotube formation, particularly focusing on the nonlinear features and size dependence of the relationship between the pulling force and membrane extraction, as well as the kinetics behaviors for the shape transitions at a molecular level. As the size of the pulling region and the membrane tension increases, the force–extraction curve becomes discontinuous and the membrane undergoes a discontinuous shape transition. A formula characterizing the nonlinear relationship between the maximum static pulling force and the size of pulling region is identified. The lipid rearrangement during the tether formation and elongation is characterized and analyzed. Moreover, our DPD simulations indicate that the steady state force is linearly proportional to the pulling velocity as well as the size of the pulling region.

2 Modeling and methods

2.1 Theoretical modeling

In the theoretical analysis, we consider an initially flat membrane patch of radius R undergoing the axisymmetric deformation induced by an external pulling force f acting on a circular nanoplate of radius r_p along the z-axis as illustrated in Fig. 1. We further restrict our attention to the quasi-static case, in which the membrane deforms and equilibrates immediately, and the total system energy can be given as[27,28,34,36]

$$E = 2\kappa \int H^2 dA + \sigma \Delta A - fL,$$

where the first term is the membrane bending energy with κ as the bending rigidity of the membrane, H as the local mean curvature, and dA as the surface element of the membrane; the second term describes the membrane tension energy with σ as the membrane tension and ΔA as the excess surface area due to the membrane extraction induced by the pulling force f; and L in the third term is the force displacement. The spontaneous
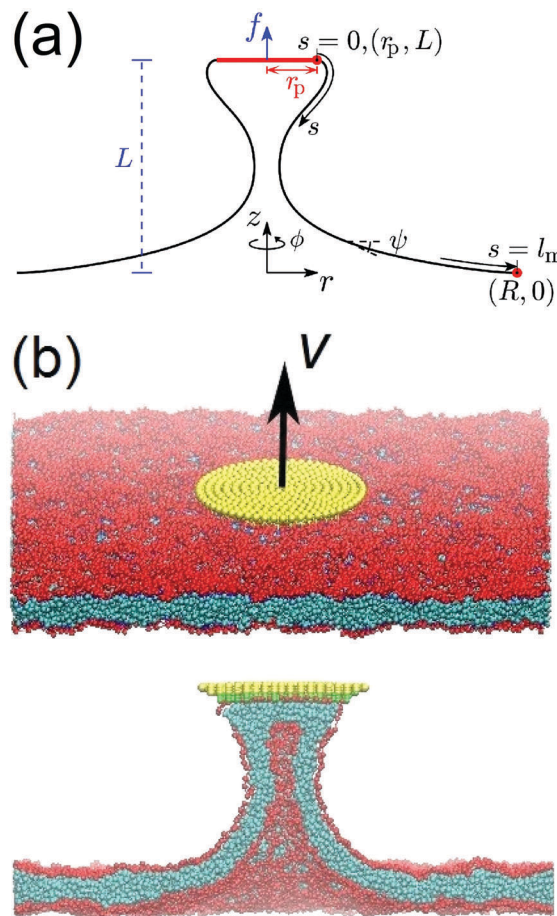
Fig. 1 (a) Schematic of a membrane tubule extraction induced by the pulling force f acting on a circular nanoplate of radius r_p in the adopted cylindrical system (r, ϕ, z). The tangent angle ψ here is positive. $r_p = 0$ corresponds to the case of the point pulling force. (b) Schematic representations of the DPD simulations models. The membrane bilayer is formed by four-bead lipids with one hydrophilic head-bead (red) and three hydrophobic tail-beads (cyan). The circular nanoplate (yellow) attached on the initially flat membrane is pulled at a velocity v along the z-direction.

curvature is not considered in our model. At a given L, f serves as a Lagrange multiplier enforcing the prescribed force displacement. Here we have omitted the energy contribution associated with the pressure jump across the membrane as it plays a negligible role in the tether formation.[13,27,28]

In the axisymmetric configuration, the mean curvature is $2H = \dot{\psi} + \sin\psi/r$, $\Delta A = 2\pi \int_0^{l_m} r ds + \pi(r_p^2 - R^2)$, and the membrane shape is determined by the tangent angle $\psi(s)$ with the geometric relations $\dot{r} = \cos\psi$ and $\dot{z} = -\sin\psi$, where l_m is the total arclength of the free membrane portion, and ψ is positive as measured clockwise from the r-axis and the dots denote derivatives with respect to the arclength s. As the total arclength l_m is unknown, we introduce a new variable $t = s/l_m$ ($t \in [0,1]$) in the free membrane region. Therefore, the system energy E can be represented as a function of the unknown variable $\psi(t)$, which is approximated by a cubic B-spline curve as $\psi(t) = \sum_{i=0}^{n} a_i N_i(t)$. The control points a_i serve as coefficients of the basis functions

This journal is © the Owner Societies 2018

Phys. Chem. Chem. Phys., 2018, 20, 3474–3483 | 3475

$N_i(t)$ defined on a non-uniform knot vector containing $n + 5$ elements ($n = 54$ in our calculations).

We employ the interior point optimization technique to numerically determine the minimum state of the membrane elastic energy at a given force displacement L. The boundary conditions provide either input parameters or equality constraints during energy minimization. At $t = 0$ (or $s = 0$), we have $\psi = 0$, $r = r_p$, and $z = L$. At the remote boundary $t = 1$ (or $s = l_m$), we have $r = R$ and $z = 0$, and we further assume that the membrane becomes flat which requires $\psi = 0$. The remote boundary condition of asymptotic flatness has been widely employed in the membrane wrapping of nanoparticles.[37] Please note that the remote boundary condition is somewhat artificial. In some theoretical work, a zero mean curvature or free hinge condition ($H = 0$) is enforced at the remote boundary.[27,28,34] The elastic energy of the membrane as a function of $\psi(t)$ under these constraints at a given L is minimized with respect to a_i and l_m. Meanwhile, the membrane configuration and the pulling force are determined at the state of the minimum elastic energy of the membrane. Hereinafter the membrane patch is taken as R in our theoretical studies unless another value is explicitly stated.

2.2 Molecular dynamics method

In our theoretical modeling, we perform the quasi-static analysis which can be used to study the membrane extraction at a sufficiently low pulling velocity v (e.g., 0.5 μm s^{-1} in ref. 35). To investigate the dynamical features and molecular mechanism of tether formation and growth, we perform molecular dynamics simulations of membrane extraction based on the dissipative particle dynamics (DPD) method,[38] which has been demonstrated to be effective and efficient in studying the mechanical behaviors of biomembranes at the mesoscale[39–45] and enables us to reveal the dynamic features of the individual molecules and membrane extraction. In DPD simulations, a cluster of atoms is represented by a bead whose dynamics is governed by Newton's equation of motion. Beads i and j interact through a simple pairwise force consisting of a conservative force ($\mathbf{F}_{ij}^C = a_{ij}\omega(r_{ij})\mathbf{n}_{ij}$), a dissipative force ($\mathbf{F}_{ij}^D = -\Gamma \omega^2(r_{ij})(\mathbf{n}_{ij}\cdot\mathbf{v}_{ij})\mathbf{n}_{ij}$), and a random force $\left(\mathbf{F}_{ij}^R = \sum \omega(r_{ij})\theta_{ij}(\Delta t)^{-1/2}\mathbf{n}_{ij}\right)$, where a_{ij} is the repulsive strength, $\mathbf{r}_{ij} = \mathbf{r}_i - \mathbf{r}_j$ (r_i being the position of bead i), $r_{ij} = |\mathbf{r}_{ij}|$, and $\mathbf{n}_{ij} = \mathbf{r}_{ij}/r_{ij}$; $\mathbf{v}_{ij} = \mathbf{v}_i - \mathbf{v}_j$ ($\mathbf{v}_i$ being the velocity of bead i), parameters Γ and Σ are related through $\Sigma^2 = 2\Gamma \, k_B T$ with 1 $k_B T = 4.14 \times 10^{-21}$ N m being the energy unit; $\theta_{ij}(t)$ is a random number with zero mean and unit variance, Δt is the time step in the unit of $\tau = (mr_c^2/\varepsilon)^{1/2}$ with m being the bead mass and ε being the energy unit; and

$$\omega(r_{ij}) = \begin{cases} 1 - r_{ij}/r_c & r_{ij} < r_c, \\ 0 & r_{ij} \geq r_c, \end{cases}$$

with r_c being the cutoff radius. $\Sigma = 3(\varepsilon^3 m/r_c^2)^{1/4}$ and $\varepsilon = 1 \, k_B T$ are taken in our simulations. The values of a_{ij} are summarized in Table S1 in the ESI.† The trajectory of beads is determined with a modified Velocity Verlet algorithm with the time step taken as $\Delta t = 0.01\tau$.[46] In the DPD simulations, the units of length, mass,

energy, and time are the cutoff radius r_c (= 1.25 nm), bead mass m (= 3.15×10^{-22} g), energy unit ε (= 1 $k_B T$), and τ (= 10.9 ps), respectively. Therefore, the units of velocity and force are derived as $\sqrt{\varepsilon/m}$ (= 1.15×10^8 μm s^{-1}) and ε/r_c (= 3.29 pN), respectively.

2.3 N-Varied DPD method

To simulate the membrane at different membrane tensions, here we employ the N-varied DPD method, which enables us to control the membrane tension by adjusting the local lipid number density in the boundary region of the simulation box.[43,47] The size of the simulation box is fixed at $60r_c \times 60r_c \times 80r_c$ with a boundary region of width $3r_c$ serving as the lipid reservoir, which surrounds a central membrane region of lateral dimensions $57r_c \times 57r_c$.

During the N-varied DPD simulations, the lipid number density ρ_{BR} in the boundary region is kept constant by adding or deleting lipids in the boundary region if ρ_{BR} deviates significantly from the prescribed value. Meanwhile, the same number of water beads are randomly deleted or added in the simulation box to keep the whole bead number density constant. In our simulations, we perform the bead addition or deletion every 1200 time steps to leave enough time for the whole membrane to avoid a state of an ill-defined membrane tension. Since the membrane tension is closely related to ρ_{BR} (see Fig. S1, ESI†), we use ρ_{BR} to specify the membrane tension in our molecular dynamics simulations. More details of the N-varied DPD method can be found in our previous work.[43,47]

2.4 DPD simulation model

Fig. 1b illustrates our coarse-grained simulation model, in which the membrane bilayer is formed by four-bead lipids with one hydrophilic head-bead (red) and three hydrophobic tail-beads (cyan).[38] The interaction between the neighboring beads in the same lipid molecule is described by a harmonic spring force with a spring constant of $100\varepsilon/r_c$ and an equilibrium bond length of $0.45r_c$. The force constraining the bond angle is described by an equilibrium angle of π and a bond bending force constant of 10ε.

The nanoplate moves as a rigid body during the simulations, and its motion provides the driving force for the membrane extraction. The lower surface of the nanoplate attracts the lipid heads of the membrane, while the upper nanoplate surface repels the lipids to avoid the penetration or internalization of the nanoplate into the membrane.[48,49] There are 1.08×10^6 beads in the simulation box with a number density of 3, and periodic boundary conditions are imposed in all three directions.

Initially, the nanoplate is placed far away from the membrane. Then a DPD simulation of 1×10^5 time steps is carried out to equilibrate the membrane at constant ρ_{BR} via lipid addition or deletion. Once the membrane reaches an equilibrium state, the nanoplate is moved gradually downwards until it comes into full contact with the membrane. Finally, a certain velocity v is imposed on the nanoplate along the z direction, extracting the membrane upwards (Fig. 1b). The canonical (NVT) ensemble is used in the simulations.

3 Results and discussion

3.1 Formation of membrane nanotube in equilibrium

Before we investigate the membrane response to a pulling force, we first examine the statics of a long bilayer tubular structure. For a cylindrical membrane nanotube of radius r and length L, the elastic membrane energy is $E_{tube} = 2\pi r L[\kappa/(2r^2) + \sigma]$. Minimizing E_{tube} with respect to r leads to the equilibrium radius $r_0 = \sqrt{\kappa/(2\sigma)}$, and the pulling force required to maintain the equilibrium configuration at L and r_0 is determined as[12,13,26–28]

$$f_0 = \partial E_{tube}\Big/\partial L = 2\pi\sqrt{2\sigma\kappa}(= 2\pi\kappa/r_0). \qquad (1)$$

This relationship connects the equilibrium force f_0, nanotube radius r_0, membrane tension σ, and the membrane bending rigidity κ, and has been used to estimate the bending rigidity and membrane tension of lipid membranes in experiments with the measurement of the nanotube radius.[9,26,30]

To investigate the membrane extraction induced by the pulling force f upon the nanoplate, we plot the normalized pulling force f/f_0 as a function of the normalized force displacement L/R in Fig. 2 and Fig. S2 (ESI†). In the early stage of membrane extraction, f increases almost linearly with the displacement L before the pulling force exceeds the equilibrium force f_0. Upon further pulling the f–L curve exhibits more deviation from the approximately linear relationship, and the pulling force f gradually rises to its maximum f_{max}. Increasing r_p or σ leads to an increasing f_{max} (Fig. 2). The proportional dependence of f_{max} on r_p has been found in the tether formation from giant vesicles with optical tweezers and the supporting Monte Carlo simulations of triangulated membrane tubules.[35] Once the force barrier f_{max} is overcome, the pulling force f drops, oscillates, and then saturates to f_0 upon the formation of a stable membrane tubular structure. At a relatively small r_p and σ, the f–L curve is smooth and continuous; while it becomes discontinuous at a large r_p (Fig. 2). Besides the f–L curves, we perform case studies on the variation of the membrane tension and bending energy during the pulling process at $\sigma = 150\kappa/R^2$

and different r_p/R (see Fig. S3, ESI†). It is shown that, though the membrane tension energy exceeds the bending energy, the bending energy of the membrane plays an increasingly important role as L/R increases. This is expected as the tension dominates in the outer region of the membrane and the bending deformation dominates in the inner membrane region.[28] The evolution of the membrane shape and the relation between f_{max} and r_p are analyzed in detail in Fig. 3 and 4, respectively.

In the case of the small membrane deformation ($L/R \ll 1$), the membrane shape can be described by the Monge parameterization $z = z(r)$. With the knowledge of $\kappa/(\sigma R^2) \ll 1$ in general, the outer region of the membrane adopts a linearized catenoidal shape with an almost zero mean curvature H.[28] The deformation of the outer membrane is dominated by the membrane tension energy as the membrane bending energy proportional to H^2 is minor, and the membrane height scales as $z \sim \ln(r/R)$. In the inner membrane region deviating from the catenoid shape, the membrane shape is determined by a balance of the bending and tension energy, and a height form $z = c_1 \ln\left(r\sqrt{\sigma/\kappa}\right) + c_2 K_0\left(r\sqrt{\sigma/\kappa}\right)$ is required to avoid divergence as $r_p \to 0$, where K_0 is the modified Bessel functions of the second kind.[28] With the introduction of another modified Bessel function K_1 of the second kind, the membrane shape at $L/R \ll 1$ could be approximately given as[28]

$$z(r) = L\frac{g(r)}{g(r_p)},$$

where $g(r) = \dfrac{r_p}{\sqrt{2}r_0}K_1\left(\dfrac{r_p}{\sqrt{2}r_0}\right)\ln\dfrac{r}{R} + K_0\left(\dfrac{r}{\sqrt{2}r_0}\right)$.

In the limit $r_p \to 0$, $z(r)$ reduces to[28]

$$z(r) = L\frac{\ln(r/R) + K_0\left[r/(\sqrt{2}r_0)\right]}{-\gamma + \ln\left(2\sqrt{2}r_0/R\right)},$$

where $\gamma = 0.5772\ldots$ is the Euler–Mascheroni constant. Further numerical calculations indicate that the above equations of $z(r)$
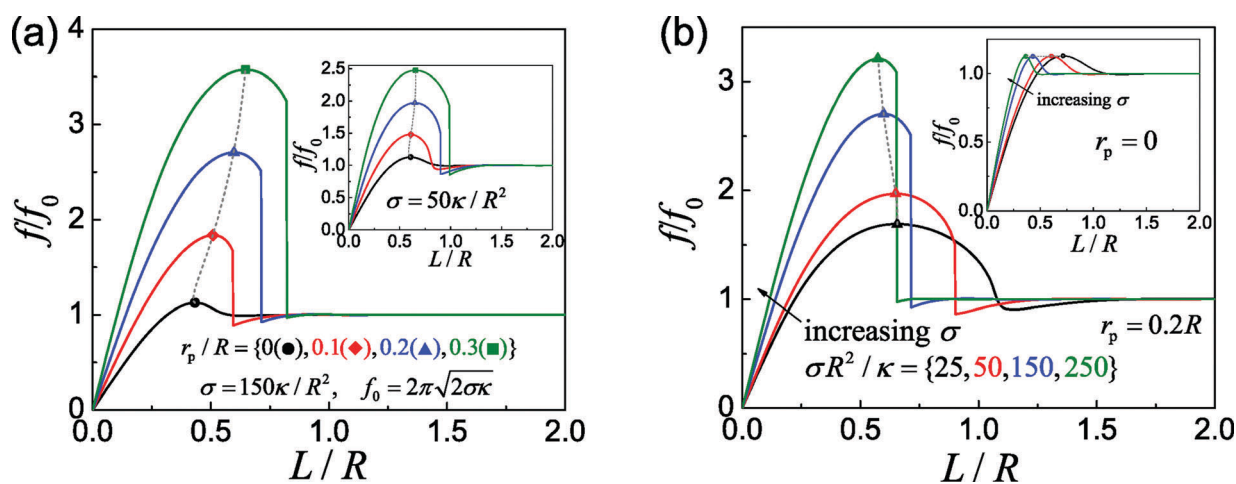
Fig. 2 Effects of the nanoplate size (a) and membrane tension (b) on the f–L curves. Solid symbols represent the maximum pulling forces f_{max}. The (grey) dashed line indicates the relationship between the maximum pulling forces and the corresponding length ratio L/R.
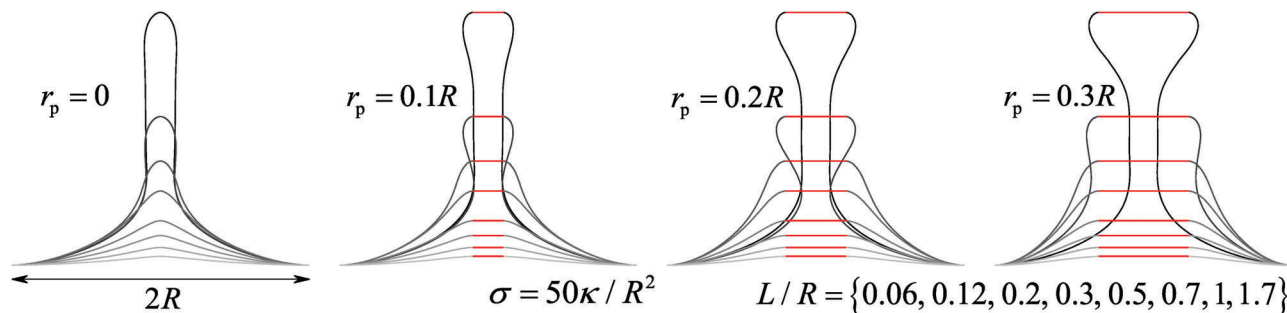
Fig. 3 Selected membrane configurations at $\sigma = 50\kappa/R^2$ and different size ratios $L/R = 0.06, 0.12, 0.2, 0.3, 0.5, 0.7, 1$, and 1.7 for $r_p/R = 0, 0.1, 0.2$, and 0.3.
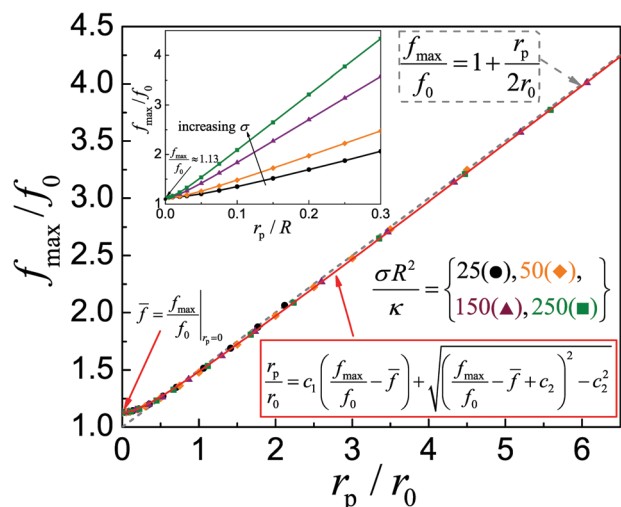
Fig. 4 Normalized maximum pulling force f_{max}/f_0 as a function of r_p/r_0 at different membrane tensions σ. Inset, f_{max}/f_0 versus the size ratio r_p/R with the equilibrium radius $r_0 = \sqrt{\kappa/(2\sigma)}$. The dashed line of the linear equation $f_{max}/f_0 = 1 + r_p/(2r_0)$ is proposed in ref. 35 and is provided here as a comparison to our present empirical relation (red solid curve).

capture the membrane deformation at $L/R \ll 1$, and the results are not shown here.

As L/R increases, the inner membrane region begins to elongate into a cylindrical nanotube, and the linearization of membrane deformation fails (Fig. 3). In the case of a point pulling force ($r_p = 0$), the tube tip is of a slightly larger radius than the cylindrical tether region; while the tube base connecting the catenoid-like outer membrane region exhibits a slight constriction (Fig. 3 and Fig. S4, ESI†). Theoretical analysis indicates that the shape of the tube tip and base can be characterized by fourth order linear differential equations for exponentially damped sinusoids.[27,28,36] As r_p increases, the tip region affected by the exponentially decaying oscillations expands, and the extracted membrane adopts a clarinet-like shape. A similar membrane configuration has also been determined in the Monte Carlo simulations of triangulated membrane tubules.[35] Moreover, the membrane extraction exhibits discontinuous shape transitions at larger L/R (Fig. 3 and Fig. S4, ESI†). This phenomenon is reflected in the f–L curves in Fig. 2a and Fig. S2 (ESI†) where the discontinuous force jump occurs at a larger L/R as r_p increases. The formation of a stable cylindrical tether

region leads to the plateau force $f_0 = 2\pi\sqrt{2\sigma\kappa}$ in Fig. 2a and Fig. S2 (ESI†). Further membrane extraction simply results in a longer cylindrical tether region without varying the geometry of the other membrane regions.

To investigate the effect of the membrane patch size on the tether formation, we perform case studies at a patch radius of $5R$ (see Fig. S5, ESI†). The ratio L/R of the maximum pulling force increases as the membrane size increases, and the smoothness of the f–L curve at finite r_p might change.

The effects of the nanoplate size on the maximum pulling force could be extracted from Fig. 2 and Fig. S2 (ESI†) for different σ. When this is done, the results are compared together in Fig. 4 and its inset. At $r_p = 0$, the force ratio f_{max}/f_0 is around 1.13, insensitive to the values of σ. At finite r_p, f_{max}/f_0 increases as σ increases (see inset in Fig. 4). Transforming r_p/R to r_p/r_0, these four separate curves collapse onto a single curve. A simple estimate of that characteristic curve based on the Monte Carlo simulations of triangulated membrane tubules is[35]

$$\frac{f_{max}}{f_0} = 1 + \frac{r_p}{2r_0},$$

which agrees well with our numerical results of continuum modeling except in the small range of $r_p/r_0 \leq 0.4$ (Fig. 4). A new empirical relation (red solid line), capable of capturing the characteristic curve f_{max}/f_0 versus r_p/r_0 in the whole range of r_p/r_0, has been found as

$$\frac{r_p}{r_0} = c_1\left(\frac{f_{max}}{f_0} - \bar{f}\right) + \sqrt{\left(\frac{f_{max}}{f_0} - \bar{f} + c_2\right)^2 - c_2^2},$$

where $c_1 = 28/29$, $c_2 = 7/17$, and $\bar{f} = (f_{max}/f_0)|_{r_p=0}$ is the force ratio f_{max}/f_0 in the case of the point pulling force which is taken as $\bar{f} = 1.1267$ here. The almost linear relationship between f_{max}/f_0 and r_p/r_0 beyond the very small region agrees well with experiments on tether extraction from vesicles[35] and 3T3 cells.[30]

3.2 Kinetics of membrane nanotube formation

To investigate the formation kinetics and molecular structure of the membrane nanotube, we perform N-varied DPD simulations as demonstrated in Fig. 1b and 5a. The nanoplate attached on the upper membrane surface is pulled at a constant pulling velocity v. The membrane is extracted and a membrane nanotube emerges and grows as the nanoplate moves upwards gradually.
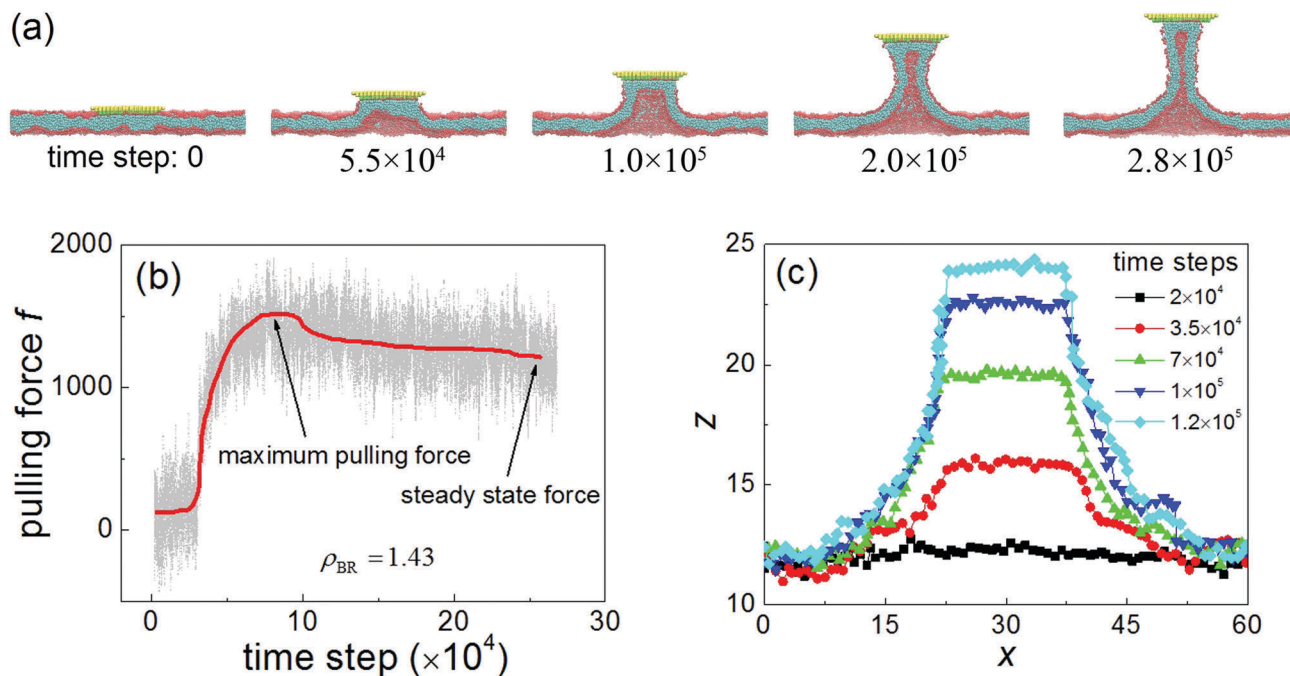
Fig. 5 (a) Morphologies of the membrane with $\rho_{BR} = 1.43$ at selected time steps during membrane extraction. (b) The pulling force as a function of the time step. (c) The midplane of the lipid membrane at different time steps from the initial membrane extraction to the tube formation. In (c) the length for the spatial unit along the vertical axis is set to be larger than that along the horizontal axis to zoom in the membrane configuration. The velocity of the nanoplate is $v = 0.01$, and its radius is $r_p = 8r_c$.

Fig. 5b shows the profile of the time- or pulling displacement-dependent pulling force f, which is defined as the conservative force exerted by the nanoplate on the membrane. Within the first 4×10^4 time steps the pulling force increases rather slowly, and then gradually rises to a maximum value in a relatively short time period (from around 4×10^4 to 7×10^4 time steps). As the simulation further proceeds, the pulling force undergoes a slight decrease and gradually saturates to a plateau value which is referred to as the steady state force in the dynamic membrane extraction. The profile of the force–displacement curve in our molecular dynamics simulations (Fig. 5b) is consistent with our theoretical analysis in Fig. 2 and Fig. S2 (ESI†) and the experimental and numerical results reported in the literature.[15,16,31] As discussed in our theoretical analysis, the drop in f is a reflection of the membrane shape transition which is captured in our molecular dynamics simulations (see Fig. 5a and c). After reaching a critical displacement of extraction (around 7×10^4 time steps), the membrane transforms from a cone-shaped protrusion to a membrane nanotube (Fig. 5a and c). A nanotube structure is formed around 9×10^4 time steps and maintained later. The DPD simulations show that the tip size of the formed nanotube is slightly larger than that of the membrane tether region and the tube base connecting the catenoid-like outer membrane region (Fig. 5a). A similar feature is characterized in our theoretical analysis in Fig. 3 and Fig. S4 (ESI†). However, we would like to point out that the DPD simulations used here suffer from the finite size effect in that the simulation box size would affect the size of membrane protrusion as well as the shape transition. This is why the sharp

shape transition predicted from the continuum theory (Fig. 2) becomes much rounded in the DPD simulations (Fig. 5).

To further understand the mechanism for the membrane tube formation at the molecular scale, we analyze our simulations in detail and focus on the variation of the average lipid number in the transition region and the membrane shape during the pulling process (see Fig. 6). The transition region is defined as the region including the most curved part of the membrane with a projection length of $15r_c$ on the horizontal plane (e.g., within the green ellipse in the inset in Fig. 6a) and the transition angle α represents the angle between the membrane profile and the horizontal plane (see the inset of Fig. 6b). As the membrane undergoes extraction, the number of lipids in the transition region increases which implies the growth of the membrane nanotube (Fig. 6a). The transition angle α fluctuates around zero degrees in the beginning of our simulations and increases sharply as the nearly flat membrane evolves to the cone-shaped structure. During the subsequent shape evolution to a membrane tether, the increment rate of the angle α slows down. As the membrane nanotube is formed, α gradually approaches $\pi/2$ (Fig. 6b). Similar trends are observed at different pulling velocities (Fig. S6, ESI†).

Fig. 7 provides the time evolutions of the membrane thickness, lipid order parameter, and lipid density in the transition region. In the early stage of the membrane extraction (0 to 4×10^4 time steps), though the membrane remains in a nearly flat configuration with thermal undulation, the thickness and lipid density of the membrane in the transition region increases quickly (Fig. 7a and b). In the meantime, the orientational order

This journal is © the Owner Societies 2018

Phys. Chem. Chem. Phys., 2018, **20**, 3474–3483 | **3479**
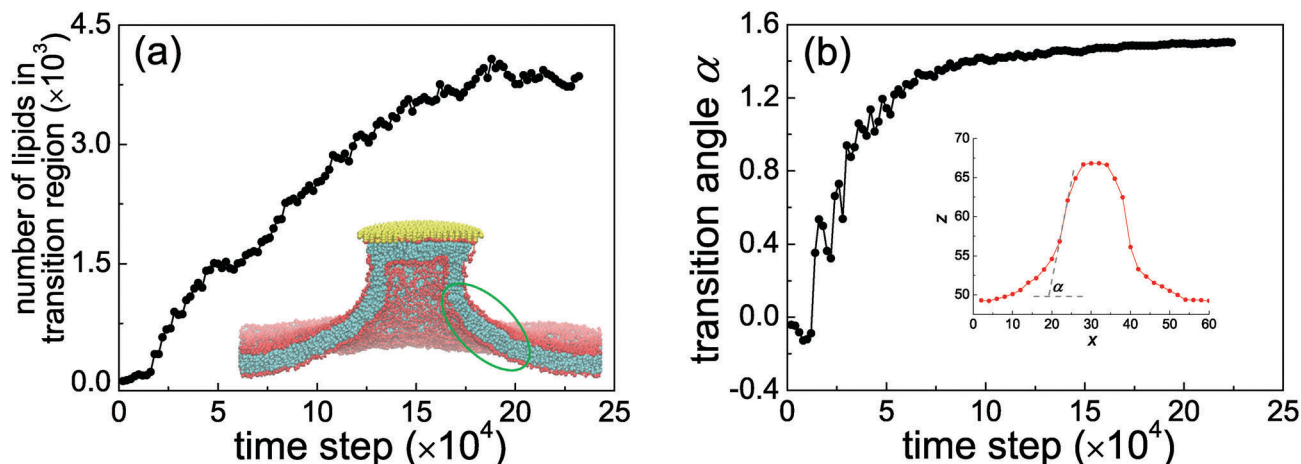
Fig. 6 (a) The amount of the lipids in the transition region (within the green ellipse in the inset in (a)) as a function of the simulation step. (b) The transition angle α varied with simulation steps (inset, the definition of the transition angle α). Here $v = 0.01$, $r_p = 8r_c$, and $\rho_{BR} = 1.43$.
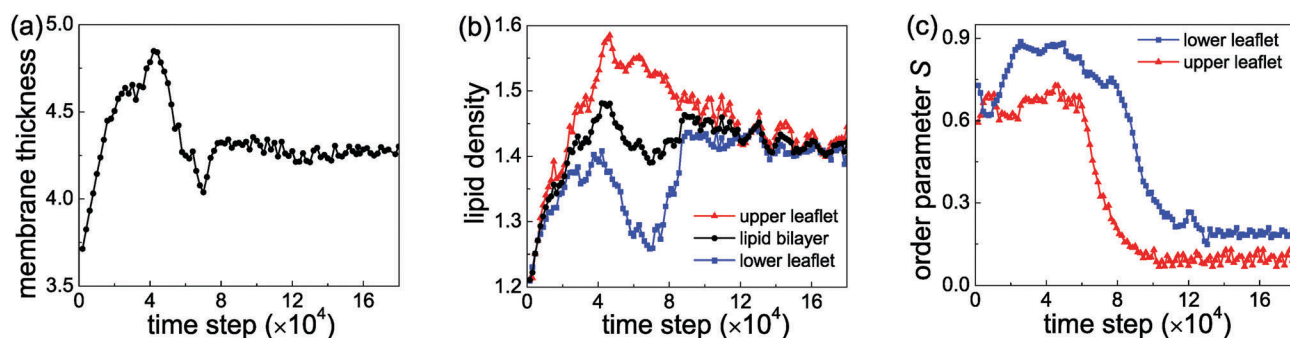
Fig. 7 Structure rearrangement of lipid molecules in the transition region during the formation of a membrane nanotube at $v = 0.01$, $r_p = 8r_c$, and $\rho_{BR} = 1.43$. (a) The average lipid bilayer thickness, (b) orientational order parameter, and (c) average lipid density of the transition region.

parameter S for lipids in the lower leaflet decreases slightly and then increases significantly, and S for the upper leaflet increases and then decreases slightly and oscillates around 0.7 (Fig. 7c). These features indicate that the lipid molecules in the lower leaflet slightly become straightened and prefer to align parallel to the z direction and the structural rearrangement of the upper leaflet is relatively weaker, meanwhile the inter-leaflet coupling is reduced and the lipid straightening causes the increase of lipid density. Here the orientational order parameter is defined as $S = \langle 3\cos^2\theta - 1\rangle/2$ with θ representing the tilt angle between the z direction and the bond vector connecting the first and third beads in the lipid tail. The brackets denote a spatial average. S is 1 as the lipids are parallel to the vertical direction, 0 as the lipids adopt a random orientation. In general, for this stage, the lipids in different leaflets show different responses to the pulling force exerted by the moving nanoplate: the upper leaflet is drawn up in response to the pulling force, while the lower leaflet is less affected. Therefore, the pulling force disturbs the membrane by reducing the inter-leaflet coupling and straightening the nearby lipids, which causes the increase of the lipid density and membrane thickness temporarily.

Upon further extraction, the membrane protrusion emerges and then the membrane develops into a cone-like shape

(around 4×10^4 to 7×10^4 time steps). The formation of a cone-shaped structure is featured by a significant increase of the pulling force (Fig. 5b), and the decrease of the lipid density and membrane thickness in the transition region (Fig. 7a and b). The decrease in the lipid density for both the upper and lower leaflets is mainly caused by the growth of the highly curved part of the membrane which accompanies the increment of the membrane area and the decrease of the membrane thickness due to area expansion. An important characteristic of this stage is that the pulling force increase sharply until it reaches the maximum (Fig. 5b), which can be understood as follows. Pulling the cone-shaped structure results in the rapid increase of the membrane area. This is one source of the rapid increase of the membrane tension energy. Besides, the dynamic simulations indicate that the large extraction speed also induces a local membrane tension gradient, since the newly increased area of the protrusion needs more lipids to maintain the given membrane tension than that could be provided by the diffusive flux of lipids from the reservoir (i.e., the boundary region in our simulations). The increase of the local membrane tension for the protrusion can be inferred from the decrease of lipid density and membrane thickness (Fig. 7a and b). Note that the membrane tension gradient depends on the speed of membrane extraction

3480 | Phys. Chem. Chem. Phys., 2018, 20, 3474–3483

This journal is © the Owner Societies 2018

and will disappear at a sufficiently slow extraction process, as in the quasi-static modeling (Fig. 3).

Within the time interval from 7×10^4 to 9×10^4 time steps, the membrane undergoes a configurational transition from a cone-shaped protrusion to a membrane tubule, with a significant change in the membrane thickness and a tendency of decreasing the lipid density in the upper leaflet and increasing the lipid density in the lower leaflet (Fig. 7b). Meanwhile, the orientational order parameter S in the upper leaflet decreases significantly, and S oscillates around 0.75 for the lower leaflet first and decreases at the end of this time interval. Overall the lipid rearrangement in the lower leaflet lags behind the upper leaflet. A continuous growth of the membrane tube is observed after 9×10^4 time steps.

With the knowledge of the f–L curve from our DPD simulations as exemplified in Fig. 5b, we can obtain the steady state force as the membrane nanotube is formed and summarize the results at different pulling velocities in Fig. 8a. It is shown that the steady state pulling force increases linearly with the pulling velocity or membrane extraction rate v at a given nanoplate size (e.g., $r_p = 8r_c$ in Fig. 8a). Though the effects of nanoplate size have not been considered in the existing literature, this linear relationship has been predicted in the theoretical analysis as[13,26]

$$f = f_t + 2\pi\eta_{eff}v, \qquad (2)$$

where f_t is the threshold force for the tether extraction to overcome the membrane bending and membrane separation from the cytoskeleton, η_{eff} is the effective viscosity of the membrane nanotube which could account for the membrane viscosity, inter-monolayer slip, and membrane slip over the cytoskeleton.[13,26] The linear relationship between η_{eff} and f in a physiological range of v has been confirmed by experimental studies[13,15,16,26] and numerical calculations.[31] Ignoring the interaction between two leaflets and the influence attributed to the cytoskeleton, f_t reduces to f_0. With the knowledge of the slope df/dv of the dashed line in Fig. 8a, we obtain the effective membrane viscosity η_{eff} as $\eta_{eff} = (df/dv)/(2\pi) = 4.55 \times 10^{-4}$ pN s μm^{-1}, which is very similar to the result for a relatively large simulated membrane (5×10^{-4} pN s μm^{-1}) obtained from the coarse-grained MARTINI model,[32] and is in agreement with the experimental data for model membranes (on the order of 1×10^{-4} pN s μm^{-1}),[11,13] but significantly smaller than the values for neuronal growth cones (0.137 pN s μm^{-1}),[26] outer hair cells (reported in a range of 2.39 pN s μm^{-1} to 5.25 pN s μm^{-1}),[16] and red blood cells (34 pN s μm^{-1})[33] due to the absence of the cytoskeleton in our simulations. Further DPD simulations indicate that the steady state force is linearly proportional to the nanoplate radius r_p (see Fig. 8b).

Eqn (1) indicates that the quasi-static tether pulling based on mechanical manipulation can be applied to measure the bending rigidity κ of the lipid membranes. Other mechanical methods for measuring κ include micropipette aspiration and electrodeformation based on the manipulation of giant unilamellar vesicles. Apart from the mechanical methods, κ can also be determined from the fluctuation analysis of a thermally excited vesicle and the small-angle X-ray scattering from membrane stacks as reviewed in ref. 50–52. Though the uncertainties in measurements are at around the 10% level, different measuring approaches employed in different research laboratories give different values of the bending rigidity.[52] In general, the fluctuation analysis gives a larger κ than those obtained from using tether pulling, micropipette aspiration, electrodeformation, or X-ray methods.[50–53] For example, the bending rigidity of the dipalmitoyl phosphatidylcholine (DMPC) membrane at around 30 °C is reported to be around 31.4 k_BT based on the shape fluctuation analysis and around 13.5 k_BT from micropipette aspiration experiments as summarized in ref. 50. The approaches of tether pulling and micropipette aspiration give a similar κ of dioleoylphosphatidylcholine (DOPC) membranes around 20 k_BT as summarized in ref. 51. More recent measurements from the same group demonstrate that the κ of membranes composed of DOPC and cholesterol are very similar as obtained by improved fluctuation analysis and vesicle electrodeformation.[53]
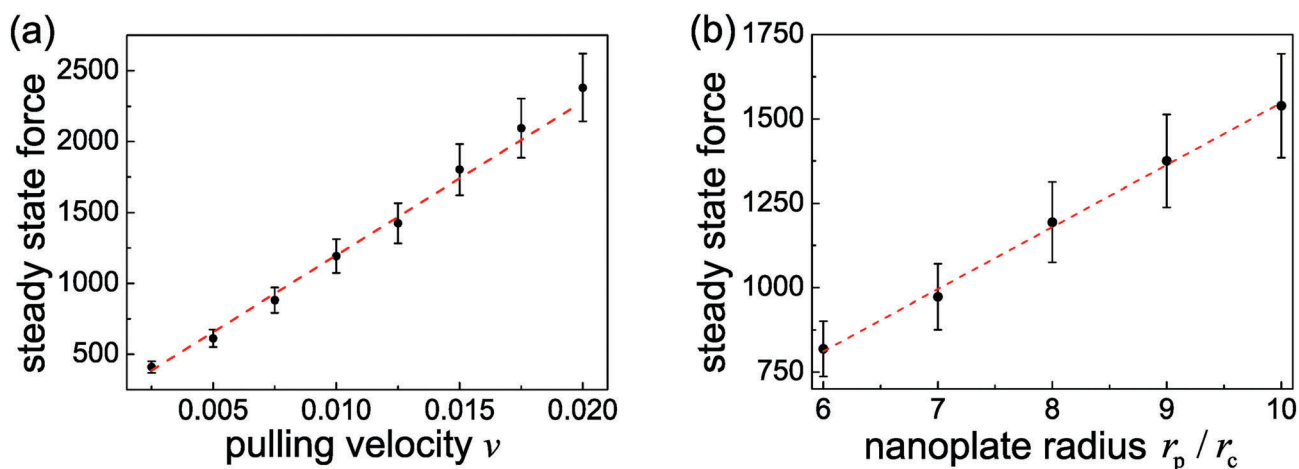
Fig. 8 (a) The steady state pulling force versus the pulling velocity v at $r_p = 8r_c$ and $\rho_{BR} = 1.43$. (b) The steady force varies as a function of the nanoplate radius at $v = 0.01$ and $\rho_{BR} = 1.43$. In this figure, the steady force was always determined after a simulation run of 2.5×10^5 time steps.

Though significant efforts have been made, very little is known about the causes of these differences in the measurement of κ.[52,53]

In the case of dynamic tether extraction, the discussions on the membrane viscosity in the previous paragraph indicate that main contributions to the variation of the measured viscosities include the membrane compositions and the presence of the underlying cytoskeleton. For a certain membrane upon dynamic extraction at a physiological rate, its viscosity η_{eff} could be determined from the linear relationship between the pulling force f and the pulling velocity v as given in eqn (2) and demonstrated in Fig. 8a.

The DPD adopted here was developed as a model to address the simulations of complex fluids and soft matter and could reach time and length scales that would be unreachable from microscopic MD simulations. In addition, it is a powerful tool to explore the generic features of systems independent of molecular specificity. Like many other simulation methods, the DPD method has unique advantages but also suffers from several limitations. For example, a DPD fluid cannot sustain a temperature gradient on hydrodynamic time scales. More detailed discussions on the merits and limitations of the DPD method could be found in a recent perspective article.[54]

4 Conclusions

We have performed theoretical analysis and DPD simulations to investigate the mechanical behavior of the membrane nanotube formation and reveal its dependence on the size of the pulling region. In the quasi-static extraction of a lipid membrane of constant membrane tension, our continuum modeling indicates that the pulling force required for the membrane extraction increases first and then drops and saturates upon the formation of a membrane nanotube. In the characteristic force–extraction curve, the maximum of the pulling force f_{max} is proportional to the membrane tension σ as well as the size of the pulling region r_{p}, and the membrane undergoes a discontinuous shape transition as σ and r_{p} increase. At finite r_{p}, f_{max} increases linearly with r_{p}; while as r_{p} approaches zero, f_{max} and r_{p} follow a nonlinear relationship. Further numerical analysis provides the energy contribution of the membrane bending and tension parts and indicates that the bending energy of the membrane plays an increasingly important role as the membrane extraction develops. A similar force–extraction curve to the continuum theoretical analysis has been obtained in our DPD simulations at finite pulling velocities, and detailed analysis indicate that the lipids in the upper and lower leaflets exhibit different behaviors of structural rearrangements during the membrane extraction. Moreover, it is shown that the steady state pulling force increases linearly with the pulling velocity as well as the size of the pulling region, and that the effective membrane viscosity has been obtained.

Our results can serve as a foundation for future studies taking into account the coupling between the cytoskeleton and membrane,[10,29,33] lipid sorting,[34] filopodial growth,[10] and cell uptake of one-dimensional nanomaterials.[55–58]

Conflicts of interest

There are no conflicts to declare.

Acknowledgements

References

1 C. Lee and L. B. Chen, *Cell*, 1988, **54**, 37–46.
2 G. Benard and R. Rossignol, *Antioxid. Redox Signaling*, 2008, **10**, 1313–1342.
3 H. H. Mollenhauer and D. J. Morre, *Histochem. Cell Biol.*, 1998, **109**, 533–543.
4 D. M. Davis and S. Sowinski, *Nat. Rev. Mol. Cell Biol.*, 2008, **9**, 431–436.
5 A. Rustom, R. Saffrich, I. Markovic, P. Walther and H.-H. Gerdes, *Science*, 2004, **303**, 1007–1010.
6 S. Sowinski, *et al.*, *Nat. Cell Biol.*, 2008, **10**, 211–219.
7 L. Ma, Y. Li, J. Peng, D. Wu, X. Zhao, Y. Cui, L. Chen, X. Yan, Y. Du and L. Yu, *Cell Res.*, 2015, **25**, 24–38.
8 P. Sundd, E. Gutierrez, E. K. Koltsova, Y. Kuwano, S. Fukuda, M. K. Pospieszalska, A. Groisman and K. Ley, *Nature*, 2012, **488**, 399–403.
9 G. Koster, M. VanDuijn, B. Hofs and M. Dogterom, *Proc. Natl. Acad. Sci. U. S. A.*, 2003, **100**, 15583–15588.
10 T. Bornschlögl, S. Romero, C. L. Vestergaarda, J.-F. Joanny, G. T. Van Nhieu and P. Bassereau, *Proc. Natl. Acad. Sci. U. S. A.*, 2013, **110**, 18928–18933.
11 R. E. Waugh, *Biophys. J.*, 1982, **38**, 29–37.
12 R. E. Waugh and R. M. Hochmuth, *Biophys. J.*, 1987, **52**, 391–400.
13 E. Evans and A. Yeung, *Chem. Phys. Lipids*, 1994, **73**, 39–56.
14 J. Dai and M. P. Sheetz, *Biophys. J.*, 1995, **68**, 988–996.
15 D. Raucher and M. P. Sheetz, *Biophys. J.*, 1999, **77**, 1992–2002.
16 Z. Li, B. Anvari, M. Takashima, P. Brecht, J. H. Torres and W. E. Brownell, *Biophys. J.*, 2002, **82**, 1386–1395.
17 B. G. Hosu, M. Sun, F. Marga, M. Grandbois and G. Forgacs, *Phys. Biol.*, 2007, **4**, 67–78.
18 M. Karlsson, K. Sott, A.-S. Cans, A. Karlsson, R. Karlsson and O. Orwar, *Langmuir*, 2001, **17**, 6754–6758.
19 M. Simunovic, G. A. Voth, A. Callan-Jones and P. Bassereau, *Trends Cell Biol.*, 2015, **25**, 780–792.
20 H. Ewers, *et al.*, *Nat. Cell Biol.*, 2010, **12**, 11–18.
21 A. Šarić and A. Cacciuto, *Phys. Rev. Lett.*, 2012, **109**, 188101.
22 A. H. Bahrami, R. Lipowsky and T. R. Weikl, *Phys. Rev. Lett.*, 2012, **109**, 188102.
23 I. Tsafrir, Y. Caspi, M.-A. Guedeau-Boudeville, T. Arzi and J. Stavans, *Phys. Rev. Lett.*, 2003, **91**, 138102.
24 Y. Li, R. Lipowsky and R. Dimova, *Proc. Natl. Acad. Sci. U. S. A.*, 2011, **108**, 4731–4736.

25 M. Staykova, D. P. Holmes, C. Read and H. A. Stone, *Proc. Natl. Acad. Sci. U. S. A.*, 2011, **108**, 9084–9088.

26 F. M. Hochmuth, J.-Y. Shao, J. Dai and M. P. Sheetz, *Biophys. J.*, 1996, **70**, 358–369.

27 I. Derényi, F. Julicher and J. Prost, *Phys. Rev. Lett.*, 2002, **88**, 238101.

28 T. R. Powers, G. Huber and R. E. Goldstein, *Phys. Rev. E: Stat., Nonlinear, Soft Matter Phys.*, 2002, **65**, 041901.

29 N. Borghi and F. Brochard-Wyart, *Biophys. J.*, 2007, **93**, 1369–1379.

30 B. Pontes, N. B. Viana, L. T. Salgado, M. Farina, V. M. Neto and H. M. Nussenzveig, *Biophys. J.*, 2011, **101**, 43–52.

31 M. Rahimi and M. Arroyo, *Phys. Rev. E: Stat., Nonlinear, Soft Matter Phys.*, 2012, **86**, 011932.

32 S. Baoukina, S. J. Marrink and D. P. Tieleman, *Biophys. J.*, 2012, **102**, 1866–1871.

33 W. C. Hwang and R. E. Waugh, *Biophys. J.*, 1997, **72**, 2669–2678.

34 H. Jiang and T. R. Powers, *Phys. Rev. Lett.*, 2008, **101**, 018103.

35 G. Koster, A. Cacciuto, I. Derényi, D. Frenkel and M. Dogterom, *Phys. Rev. Lett.*, 2005, **94**, 068101.

36 B. Božic, V. Heinrich, S. Svetina and B. Žekš, *Eur. Phys. J. E: Soft Matter Biol. Phys.*, 2001, **6**, 91–98.

37 X. Yi, X. Shi and H. Gao, *Phys. Rev. Lett.*, 2011, **107**, 098101.

38 M. Laradji and P. B. S. Kumar, *Phys. Rev. Lett.*, 2004, **93**, 198105.

39 J. C. Shillcock and R. Lipowsky, *Nat. Mater.*, 2005, **4**, 225–228.

40 K. Yang and Y. Q. Ma, *Nat. Nanotechnol.*, 2010, **5**, 579–583.

41 J. Gao, S. Li, X. Zhang and W. Wang, *Phys. Chem. Chem. Phys.*, 2010, **12**, 3219–3228.

42 S. Li, X. Zhang and W. Wang, *Biophys. J.*, 2010, **98**, 2554–2563.

43 T. Yue and X. Zhang, *Soft Matter*, 2011, **7**, 9104–9112.

44 H.-M. Ding, W.-D. Tian and Y.-Q. Ma, *ACS Nano*, 2012, **6**, 1230–1238.

45 R. Guo, J. Mao and L.-T. Yan, *ACS Nano*, 2013, **7**, 10646–10653.

46 R. D. Groot and P. B. Warren, *J. Chem. Phys.*, 1997, **107**, 4423–4435.

47 F. Tian, X. Zhang and W. Dong, *Phys. Rev. E: Stat., Nonlinear, Soft Matter Phys.*, 2014, **90**, 052701.

48 R. S. Dias, A. A. C. C. Pais, P. Linse, M. G. Migue and B. Lindman, *J. Phys. Chem. B*, 2005, **109**, 11781–11788.

49 Y. Li, *Phys. Chem. Chem. Phys.*, 2014, **16**, 12818–12825.

50 D. Marsh, *Chem. Phys. Lipids*, 2006, **144**, 146–159.

51 J. F. Nagle, *Faraday Discuss.*, 2013, **161**, 11–29.

52 J. F. Nagle, M. S. Jablin, S. Tristram-Nagle and K. Akabori, *Chem. Phys. Lipids*, 2015, **185**, 3–10.

53 R. S. Gracia, N. Bezlyepkina, R. L. Knorr, R. Lipowsky and R. Dimova, *Soft Matter*, 2010, **6**, 1472–1482.

54 P. Español and P. B. Warren, *J. Chem. Phys.*, 2017, **146**, 150901.

55 R. Vácha, F. J. Martinez-Veracoechea and D. Frenkel, *Nano Lett.*, 2011, **11**, 5391–5395.

56 X. Shi, A. von dem Bussche, R. H. Hurt, A. B. Kane and H. Gao, *Nat. Nanotechnol.*, 2011, **6**, 714–719.

57 X. Yi, X. Shi and H. Gao, *Nano Lett.*, 2014, **14**, 1049–1055.

58 W. Zhu, A. von dem Bussche, X. Yi, Y. Qiu, Z. Wang, P. Weston, R. H. Hurt, A. B. Kane and H. Gao, *Proc. Natl. Acad. Sci. U. S. A.*, 2016, **113**, 12374–12379.

This journal is © the Owner Societies 2018

Phys. Chem. Chem. Phys., 2018, **20**, 3474–3483 | **3483**

Supporting Information for "Size-dependent formation of membrane nanotubes: Continuum modeling and molecular dynamics simulations"

Falin Tian, Tongtao Yue, Wei Dong, Xin Yi,[*] and Xianren Zhang[*]

E-mail: xyi@pku.edu.cn; zhangxr@mail.buct.edu.cn

The parameters a_{ij} chosen for the DPD simulations are in the unit of $\varepsilon/r_{\mathrm{c}}$, where ε is the energy unit and r_{c} is the cutoff radius for the interaction. Values of a_{ij} can be found in Table S1.

Table S1: Values of interaction parameter a_{ij} between two beads in DPD simulations.

	lipid head	lipid tail	lower surface of nanoplate	upper surface of nanoplate	water
lipid head	25	200	10	30	25
lipid tail	200	25	200	200	200
low surface of nanoplate	10	200	25	25	30
upper surface of nanoplate	30	200	25	25	25
water	25	200	30	25	25
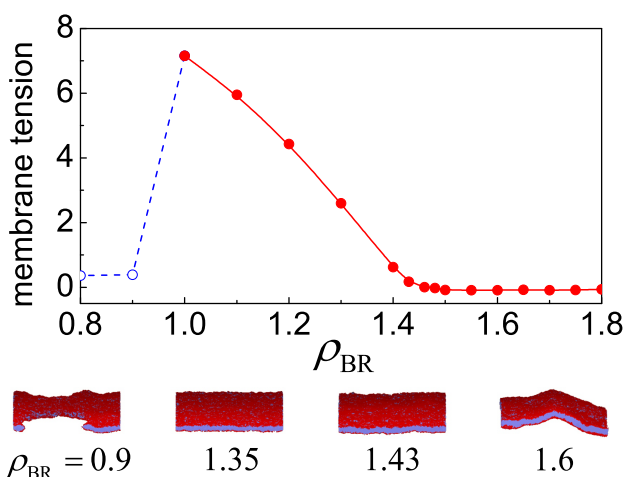
Figure S1: The membrane tension as a function of the lipid number density ρ_{BR}, and selected membrane morphologies at different $\rho_{\mathrm{BR}} = 0.9$, 1.35, 1.43, and 1.6. The lipid membrane would rapture at ρ_{BR} ranging from 0.8 to 1.0.

To investigate the relationship between the membrane tension and the lipid number density, we perform N-varied DPD simulations and calculate the membrane tension as a function of lipid number density in the boundary region ρ_{BR} as shown in Fig. S1. The lipid membrane ruptures and

---

[*]To whom correspondence should be addressed

a hole forms at $\rho_{BR} < 1.0$. As ρ_{BR} increases from 1.0 to 1.45, membrane tension decreases. As Fig. S1 indicates, ρ_{BR} corresponding to a tensionless membrane is around 1.43. At $\rho_{BR} > 1.5$, the membrane tension becomes negative, and the membrane undergoes strong fluctuation. In the present work, we consider lipid membranes of $\rho_{BR} = 1.33$, 1.43, and 1.53, which correspond to a positive membrane tension, zero membrane tension, and negative membrane tension, respectively.

To analyze the effects of r_p/R on the pulling force, we compare f-L curves with $\sigma = 250\kappa/R^2$ at different ratios r_p/R in Fig. S2. As r_p/R increases, the ratio f/f_0 increases and the f-L curve evolves from a smooth and continuous curve at $r_p = 0$ to a curve exhibiting discontinuous evolution. Similar feature is observed in Fig. 2a at $\sigma = 50\kappa/R^2$ and $150\kappa/R^2$.
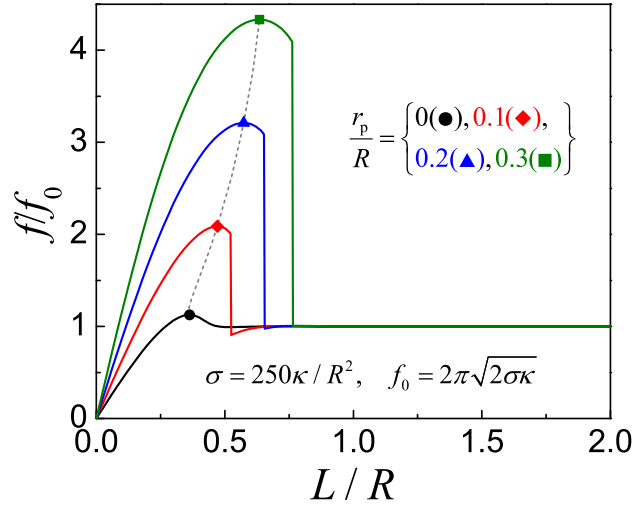
Figure S2: The f-L curves at $\sigma = 250\kappa/R^2$ and different nanoplate sizes of $r_p/R = 0$, 0.1, 0.2, and 0.3. Solid symbols represent the maximum pulling forces. The (grey) dashed line indicates the relationship between the maximum pulling forces and the corresponding length ratio L/R.
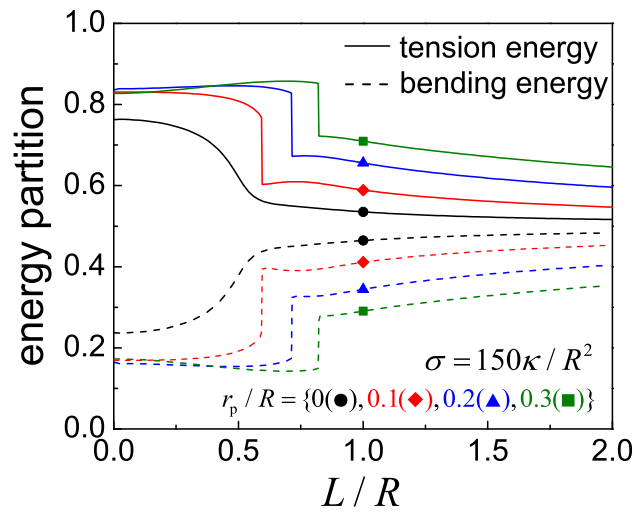
Figure S3: Variations of the membrane tension and bending energy as a function of L/R at $\sigma = 150\kappa/R^2$ and different nanoplate sizes.

2

Besides the f-L curves, we are also interested in the variation of the membrane tension and bending energy during the pulling process. In Fig. S3, we perform case studies on their variation as a function of L/R at $\sigma = 150\kappa/R^2$. In the early stage of the membrane extraction, tension dominates the membrane deformation and suppresses the large deformation of the membrane. Therefore, no tubule structure but only a cone-shaped configuration is adopted by the extracted membrane. As L/R increases, the bending energy of the membrane plays an increasingly important role as a membrane tubule is formed, though the tension energy still exceeds the bending energy.
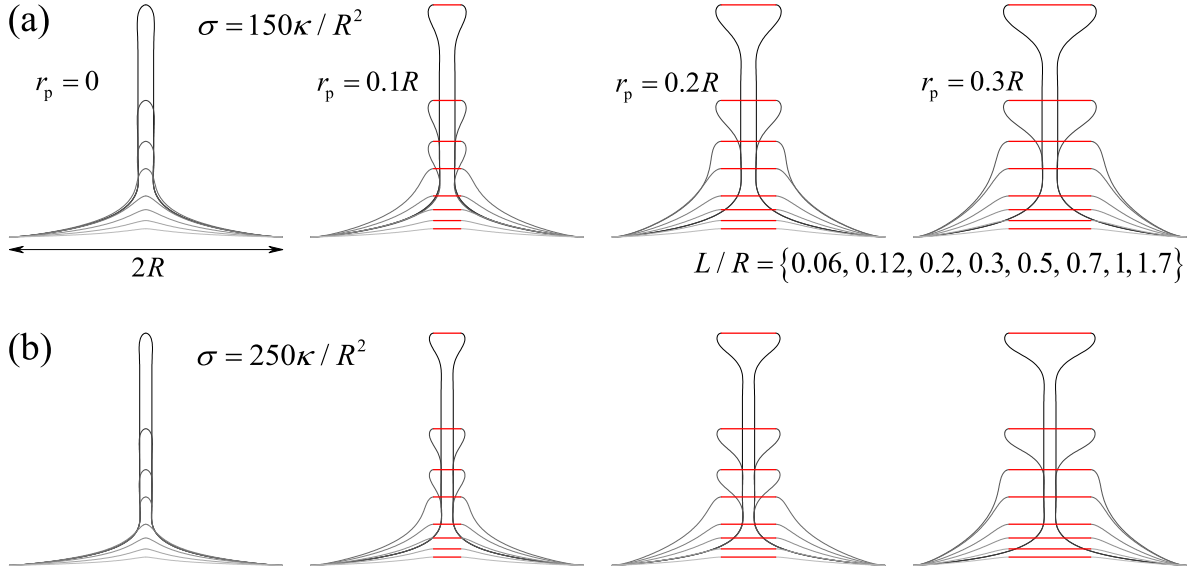
Figure S4: Selected membrane configurations at $L/R =0.06$, 0.12, 0.2, 0.3, 0.5, 0.7, 1, and 1.7, and different membrane tension $\sigma = 150\kappa/R^2$ (a) and $250\kappa/R^2$ (b) for $r_p/R = 0$, 0.1, 0.2, and 0.3.

The membrane configurations at $\sigma = 50\kappa/R^2$ are provided in Fig. 3 in the main text. Here we plot the configurations at $\sigma = 150\kappa/R^2$ and $250\kappa/R^2$ in Fig. S4a and S4b, respectively. In the case of a point pulling force ($r_p = 0$), the membrane transition as a function of L/R is smooth. As r_0 increases, a discontinuous shape transition is observed. This is consistent with f-L curves in Figs. 2a and S2, where discontinuous force jumps are observed at the finite values of r_p/R. A comparison between Figs. 3 and S4 indicates that a larger membrane tension corresponds to a smaller tether radius independent of r_p, which is expected from the formula $r_0 = \sqrt{\kappa/(2\sigma)}$.

In the main text, the radius of the membrane patch is taken as R. To investigate the effect of the membrane patch size on the tether formation, we perform case studies at the patch radius of $5R$. As shown in Fig. S5, the ratio L/R of the maximum pulling force increases as the membrane size increases but the static pulling force $f_0 = 2\pi\sqrt{2\sigma\kappa}$ is independent of the membrane patch size. As the membrane size increases from R to $5R$, the f-L curve at $r_p = 0.2R$ and $\sigma = 25\kappa/R^2$ evolves from a smooth and continuous curve to a curve exhibiting discontinuous transition.

In Fig. 6 in the main text, we investigate the variation of the lipid number in the transition region and the membrane shape during the pulling process at $v = 0.01$. To explore the effects of pulling velocity on the lipid rearrangement in the transition region and the membrane shape, we calculate the number of lipids in the transition region and the transition angle at different pulling velocities (Fig. 6b and 6c). A larger pulling velocity results in a more rapid nanotube growth (Fig. S6a) and quicker variation of the transition angle (Fig. S6b).
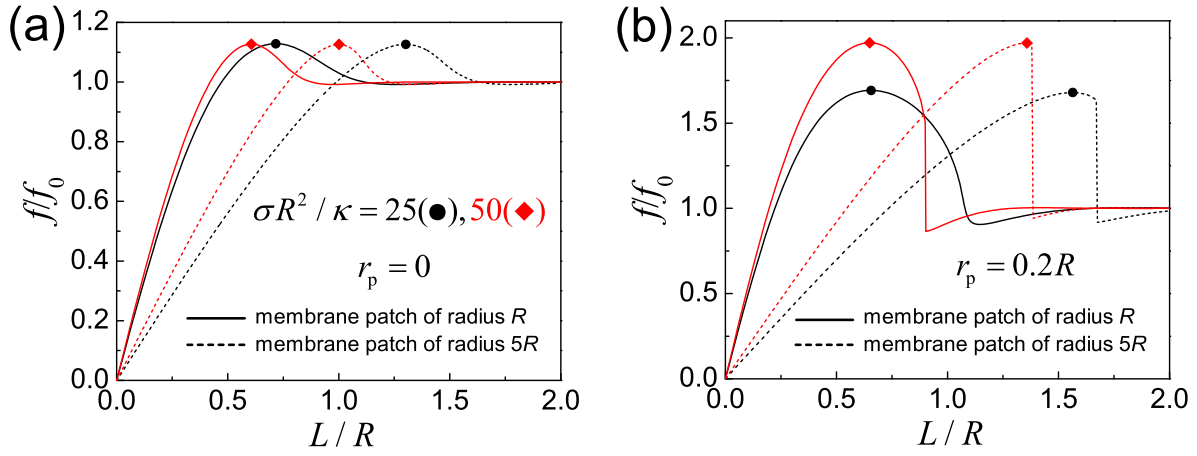
Figure S5: The f-L curves at different membrane sizes and different nanoplate sizes of $r_{\mathrm{p}} = 0$ (a) and $0.2R$ (b). The solid symbols represent the maximum pulling forces.
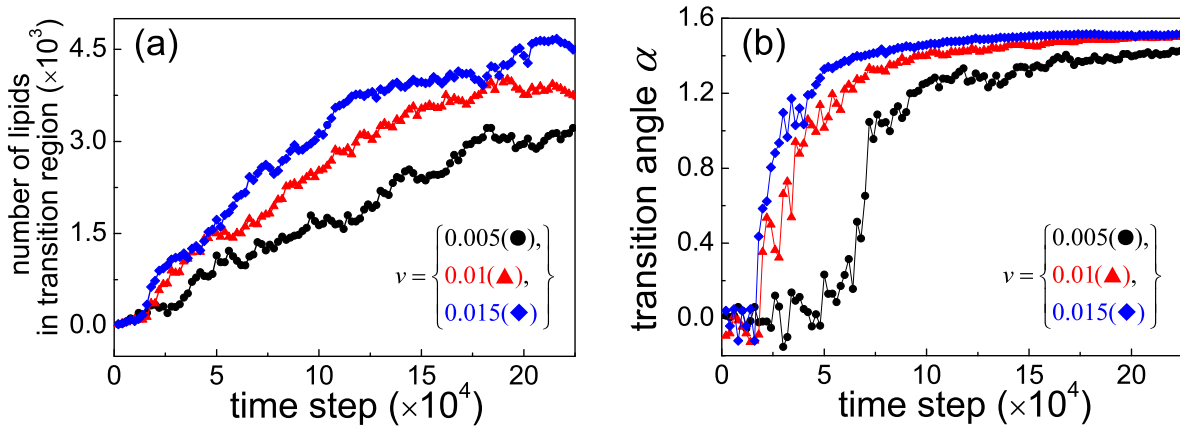
Figure S6: The number of lipids in the transition region and the transition angle α as functions of the time steps at three different pulling velocities $v = 0.005$, 0.01, and 0.015. Here $r_{\mathrm{p}} = 8r_{\mathrm{c}}$ and $\rho_{\mathrm{BR}} = 1.43$.